ACS SENSORS

Article

pubs.acs.org/acssensors

Nanoantenna-Enhanced Infrared Spectroscopic Chemical Imaging

Lucca Kühner,[†] Mario Hentschel,[†] Ute Zschieschang,[‡] Hagen Klauk,[‡] Jochen Vogt,[§] Christian Huck,[§] Harald Giessen,[†] and Frank Neubrech*[,†,§]

[†]4th Physics Institute and Research Center SCoPE, University of Stuttgart, Pfaffenwaldring 57, 70569 Stuttgart, Germany

[‡]Max Planck Institute for Solid State Research, Heisenbergstraße 1, 70569 Stuttgart, Germany

[§]Kirchhoff Institute for Physics, Heidelberg University, Im Neuenheimer Feld 227, 69120 Heidelberg, Germany

Supporting Information

ABSTRACT: Spectroscopic infrared chemical imaging is ideally suited for label-free and spatially resolved characterization of molecular species, but often suffers from low infrared absorption cross sections. Here, we overcome this limitation by utilizing confined electromagnetic near-fields of resonantly excited plasmonic nanoantennas, which enhance the molecular absorption by orders of magnitude. In the experiments, we evaporate microstructured chemical patterns of C_{60} and pentacene with nanometer thickness on top of homogeneous arrays of tailored nanoantennas. Broadband mid-infrared spectra containing plasmonic and vibrational information were acquired with diffraction-limited resolution using a two-dimensional focal plane array detector. Evaluating the enhanced infrared absorption at the respective frequencies, spatially resolved chemical images were obtained. In these chemical images, the microstructured chemical patterns are only visible if nanoantennas are used. This confirms the superior performance of our approach over conventional spectroscopic infrared imaging. In addition to the improved sensitivity, our technique provides chemical selectivity, which would not be available with plasmonic imaging that is based on refractive index sensing. To extend the accessible spectral bandwidth of nanoantenna-enhanced spectroscopic imaging, we employed nanostructures with dual-band resonances, providing broadband plasmonic enhancement and sensitivity. Our results demonstrate the potential of nanoantenna-enhanced spectroscopic infrared chemical imaging for spatially resolved characterization of organic layers with thicknesses of several nanometers. This is of potential interest for medical applications which are currently hampered by state-of-art infrared techniques, e.g., for distinguishing cancerous from healthy tissues.

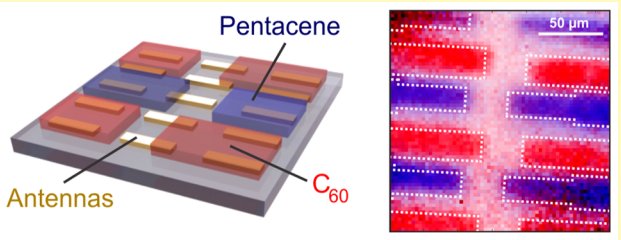

KEYWORDS: *surface-enhanced infrared spectroscopy, infrared chemical imaging, plasmonic, nanoantennas, refractive index sensing*

Infrared (IR) spectroscopy is a powerful tool for label-free, nondestructive, and unambiguous identification and characterization of molecular species and their conformational structure. Such information is extracted from material-specific IR vibrations,[1] located mainly in the fingerprint region (500 to 1500 cm^{-1}) but also between 1500 and 4000 cm^{-1} (mainly stretching vibrations of single, double, and triple bonds). This method enables applications such as environmental and industrial monitoring, security screening, medical diagnosis, or chemical imaging.[2−4]

IR chemical imaging, for example, is often applied in combination with diffraction-limited microscopic IR spectroscopy (microspectroscopy) and provides spatially resolved and material-specific information on microstructured samples.[5,6] This is of special interest in medicine and biology for the discrimination between healthy tissues and tumors[7] of unstained biological tissue sections.[8]

Unfortunately, the IR absorption cross sections, which are exploited to identify the respective materials and generate the chemical images, are relatively small. This is of minor importance for conventional IR spectroscopy of extended molecular films where many molecules contribute to the vibrational signal, since large apertures can be used. In such experiments (e.g., in IR reflection absorption spectroscopy, IRRAS), monolayer sensitivity is reached. However, laterally resolved spectroscopic IR imaging, with resolutions and aperture sizes close to the diffraction limit, suffers from the low IR absorption. This hampers imaging of nanometer-thick tissues with widely used standard Fourier-transform infrared (FTIR) spectrometers employing thermal light sources. Advanced light sources, such as synchrotrons, provide higher sensitivity but are not easily accessible.[9−11] Additionally, hyperspectral IR chemical imaging with lateral resolution at the diffraction limit is still hampered by the synchrotron's low intensity, even when focal plane array (FPA) detectors are used. Such detectors record up to 128 × 128 spectra simultaneously, which results in drastically reduced acquisition times compared to conventional scanning techniques. Laser-based approaches, e.g., using quantum cascade lasers, provide more intense IR radiation but suffer from a narrowband emission that prevents

Received: February 3, 2017
Accepted: April 24, 2017
Published: April 24, 2017

DOI: 10.1021/acssensors.7b00063
ACS Sens. 2017, 2, 655−662

spectroscopic imaging.[12−14] Recently, it was demonstrated that wavelength-sweeping techniques may improve this situation.[15]

We demonstrate in this paper that the use of resonant plasmonic nanoparticles can overcome these limitations and enable spectroscopic IR chemical imaging. As a matter of fact, plasmonic nanoantennas confine electromagnetic radiation on the nanometer scale.[16] Such enhanced near-fields have been exploited to increase the performance of different spectroscopic methods, for example, enhanced fluorescence,[17] surface-enhanced Raman spectroscopy (SERS),[18−20] or surface-enhanced IR spectroscopy (SEIRA).[21−23] For the latter, a variety of tailored nanostructures, such as wire gratings,[24] linear antennas,[25] nanoslits,[26] or more complex objects,[27−31] were used to enhance the IR vibrations of molecules and phonons by up to 5 orders of magnitude.[32] In contrast to conventional SEIRA using inhomogeneous and randomly arranged metal island films,[33,34] the use of *resonantly tuned* nanostructures provides significantly higher sensitivity. More importantly, state-of-the-art nanofabrication techniques such as electron-beam lithography or direct laser writing[35] allow for the homogeneous preparation of large arrays of tailored nano-antennas, which is a prerequisite for spatially resolved chemical imaging. Moreover, the plasmonic near-fields and thus the SEIRA enhancement are localized within a distance of 100 nm from the antenna surface, enabling ultrasensitive chemical imaging of nanometer-thick molecular layers.[36] This implies that only vibrations of molecules located in the hotspots of antennas are enhanced. No enhancement is found for molecules located outside the plasmonic hotspots, resulting in a sparse sampling. However, since conventional far-field IR chemical imaging is diffraction-limited and micropatterns with dimensions larger than the diffraction limit are imaged in our experiments, the effect has no consequences for our measurements.

In contrast to a previous study where SEIRA was combined with IR chemical imaging to detect vibrational bands of only one molecular species, namely, poly(methyl methacrylate) (PMMA),[37] we apply this concept to enhance different vibrational bands of two different materials by single and multiresonant structures. Consequently, spatially and chemically resolved identification of microstructured molecular patterns has been demonstrated in our experiments. More specifically, we employed stencil mask lithography[38,39] to cover homogeneous arrays of tailored gold nanoantennas with microstructured patterns of C_{60} and pentacene molecules. The molecular patterns, as obtained from the material-specific IR vibrations, are clearly visible if nanoantennas are used. We show that this approach is superior to refractive index sensing, which only allows for unspecific material detection. Additionally, dolmen-shaped nanostructures with dual-band plasmonic resonances were employed to broaden the accessible bandwidth of nanoantenna-enhanced spectroscopic imaging substantially. The use of dual-band as well as single-band antennas will not lower the spatial resolution when compared to conventional IR chemical imaging, since the nanostructures are substantially smaller than the imaging wavelength.

In a first series of experiments, we use linear gold nanostructures featuring a single plasmonic resonance to enhance the molecular vibrations of pentacene and C_{60} in order to demonstrate spectroscopic chemical IR imaging. Our experimental concept is schematically illustrated in Figure 1. The plasmonic resonance of our nanoantenna is designed to overlap with a characteristic vibrational mode of pentacene as well as C_{60}. Due to the coupling of the molecular vibration to the antenna resonance, a clear vibrational feature is visible in the far-field response of the antennas. As sketched in Figure 1 this material-specific vibration of the molecule makes it possible to infer on the presence of that particular molecular species inside the near-field volume of the nanoantennas. The far-field spectra of the antennas can therefore be used for the identification of the molecular species that are present at the spatial location at which the spectrum was recorded. In our proof-of-concept experiments, we resolve the spatial distribution of evaporated microstructured and nanometer-thick films of pentacene and C_{60}, indicated as the red and blue patches in Figure 1. The relative distribution on top of the nanoantenna array is known due to the design of the stencil that was used in the evaporation process of the molecular layers. Recording the spectra of the antennas over the entire array thus permits construction of a chemical image of the sample by utilizing material-specific vibrations of the molecular species, as sketched in the lower part of the figure.

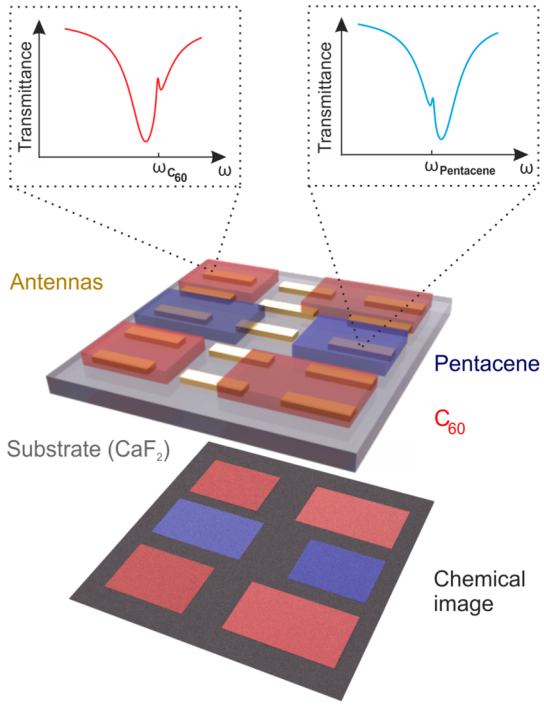

Figure 1. Nanoantenna-enhanced IR chemical imaging (schematic drawings). Surface-enhanced IR absorption spectroscopy refers to the resonant interaction of a plasmonic nanoantenna with a vibrational mode of a nearby molecular species. The far-field spectrum of such hybrid structures then contains the characteristic vibrations of the specific molecules, as sketched in the upper part of the figure. These characteristic signatures allow for resolving the known spatial distribution of thin layers with thicknesses of several tens of nanometers of two distinct molecular species. In our model system, pentacene and C_{60} are deposited in a microstructured fashion (typically 100 × 100 μm^2), as illustrated in the center of the figure. Extracting the strength of the vibrational mode for different spectra taken over the entire region of interest allows drawing a chemical map of the spatial distribution of the molecular species.

EXPERIMENTAL SECTION

Arrays of linear and dolmen-shaped gold nanoantennas are prepared on IR transparent calcium fluoride (CaF_2) substrates with a size of 1 × 1 cm^2 and a thickness of 1 mm via standard electron beam lithography (Raith eLINE Plus) using a double layer poly(methyl methacrylate)

DOI: 10.1021/acssensors.7b00063
ACS Sens. 2017, 2, 655−662

resist (200 kDa and 950 kDa, Allresist). In order to dissipate electric charge on the insulating substrates, we utilize a commercially available conductive polymer (espacer, ShowaDenko) which is applied via spin coating and is removed in water prior to development. After development, a 2-nm-thick Cr (for adhesion) and an 80-nm-thick Au layer are thermally evaporated followed by a lift-off procedure in an *N*-ethyl-2-pyrrolidone (NEP) based remover (Allresist). The lateral size of the final arrays on the substrate is 4 × 4 mm^2. As we want to carefully map the spatial distribution of our molecular species, excellent homogeneity of the antennas is essential for our imaging application. The size, shape, and other geometrical parameters crucially influence the resonance behavior of the particles and might mask the desired vibrational feature if the resonance position of the antennas is a strong function of the location on the sample. A slightly varied resonance frequency will result in differently enhanced molecular vibrations,[40] generating artifacts in the chemical images, e.g., spurious intensity gradients. The rectangular cross sections of the linear antennas are 80 nm × 100 nm with a length of 2.3 μm in order to match the plasmon resonance to the vibrational bands of the investigated molecules, as shown on top of Figure 1. Additionally, the periodicities parallel and perpendicular to the antennas' long axis (3.3 and 3.9 μm, respectively) are optimized to excite Rayleigh modes for further enhancement of the molecular vibrations.[41]

As a second step, 30 nm (for single band antennas) and 100 nm (for dual band antennas) thick micron-scale spatially discrete films of pentacene and C_{60} are thermally evaporated via stencil mask lithography to obtain spatially separated molecular patterns.[38,39] Since the deposition of high-quality pentacene layers requires that the substrate is held at an elevated temperature during the deposition,[42] whereas the C_{60} layers should not be exposed to elevated temperatures during or after the deposition, the pentacene layer was deposited first, with the substrate held at a temperature of 60 °C, followed by the deposition of the C_{60} layer, with the substrate at room temperature. As the lateral alignment accuracy of the subsequent evaporation steps is limited, overlap of the microstructured C_{60} and pentacene cannot always be avoided, which is, however, not limiting our measurements. Typically, these structures are deposited via evaporation in high vacuum ($<10^{-5}$ mbar) at a substrate temperature of 25 °C with a rate of 0.2 to 0.8 Å/s for C_{60} and at 60 °C with a rate of 0.15 to 0.35 Å/s for pentacene. Based on the evaporation rates the layer thickness is calculated and verified by fitting the dielectric function of pentacene and C_{60} known from the literature to the measured transmittance. Since the two molecular species feature several different vibrational modes in the mid-IR fingerprint region, the spectral width of a single-band antenna is in general sufficient for an unambiguous identification of these two different molecular species. This holds particularly true for our chosen model system of pentacene and C_{60}, making the microstructured pattern ideally suited as model system for an arbitrary distribution of any other molecular specimen.

In order to reconstruct the spatial distribution of the molecular species it is necessary to record spatially resolved spectra. The IR optical data are acquired with a standard FTIR spectrometer (Bruker Vertex 80v) coupled to an IR microscope (Bruker IRscope II) which is equipped with a thermal light source (globar). The crucial addition to the setup is a mercury cadmium telluride (MCT) focal plane array (FPA) detector consisting of 64 × 64 pixels. For a given magnification of 15× with a numerical aperture of 0.52 and a focal pixel size of 2.5 μm, the detector images an area of 171 μm × 171 μm. The imaging resolution is restricted by the diffraction limit. Within the sampled area, the FPA detector records the IR transmittance for each of these pixels simultaneously. For a complete chemical map, 4096 spectra are recorded and normalized to a bare CaF_2 wafer as reference. Sample and reference spectra over a spectral range of 1000 to 4000 cm^{-1} are taken with a spectral resolution of 4 cm^{-1} and 1000 scans (corresponding to approximately 1 h acquisition time) each. In contrast, conventional chemical maps acquired with a single element (one pixel) detector and scanning techniques take roughly 300 times longer acquisition as compared to the FPA detector employed here.

RESULTS AND DISCUSSION

Representative relative transmittance spectra (normalized to a bare CaF_2 wafer) of selected pixels are shown in Figure 2a for

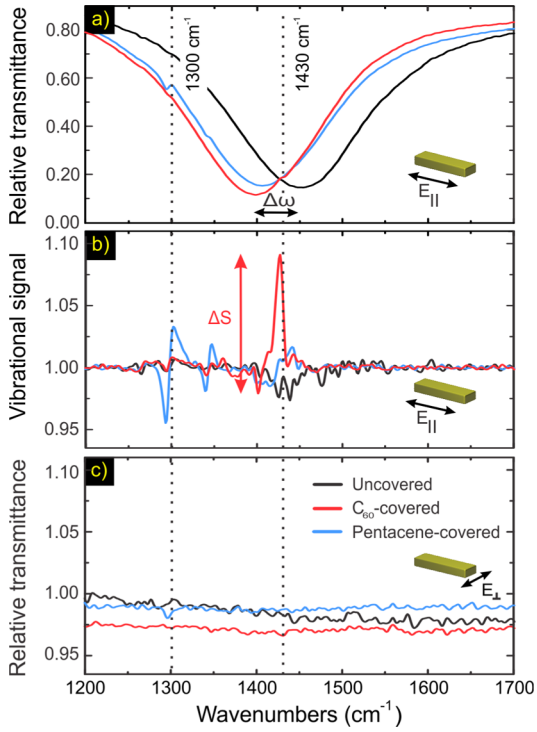

Figure 2. Nanoantenna-enhanced molecular vibrations of C_{60} and pentacene. (a) Three representative transmittance spectra of our samples (excitation along the long axis of the antennas): Uncovered antennas (black), antennas covered with 30-nm-thick films of pentacene (blue), and C_{60} (red). The overcoat leads to a resonance redshift ($\Delta\omega$) due to the higher effective refractive index. Additionally, the spectra of the covered antennas exhibit the clear vibrational features which are characteristic for pentacene at 1300 cm^{-1} and C_{60} at 1430 cm^{-1}. (b) Baseline-corrected vibrational signal spectra. In the overcoated case one can clearly see the enhanced signal strength ΔS (peak-to-peak value) at the characteristic spectral positions. No cross-talk is observed, and the bare antennas show a featureless response, as expected. (c) Control experiment for off-resonant excitation of the plasmon mode. For perpendicularly polarized ($E_\perp$) incident light, no plasmon mode is observed, and the transmittance spectra lack of vibrational fingerprints. These findings demonstrate the larger detection efficiency of the antenna-enhanced scheme. It is noteworthy that the molecular films are too thin to be detected without plasmonic enhancement.

three different positions on the molecule-covered antenna sample. The incoming light field is polarized parallel to the long axis of the antennas in order to excite the fundamental plasmonic resonance. The blue and red curves correspond to pentacene- and C_{60}-covered areas, respectively, whereas the black curve displays an uncovered area. Two main features are clearly visible: First, the plasmonic resonance undergoes a redshift when the antennas are covered with the molecular layer. This is caused by the increased effective refractive index of the surrounding medium. Second, one can identify two characteristic vibrations in the transmittance spectra of the covered antennas at 1300 cm^{-1} in the case of pentacene and 1430 cm^{-1} in the case of C_{60}. It is also noteworthy that no crosstalk between the two molecular species is observed, underlining that it is indeed possible to identify the spatial

DOI: 10.1021/acssensors.7b00063
ACS Sens. 2017, 2, 655−662

distribution of the molecular species from the far-field spectrum.

Both these features can be utilized to create a map of the sample. If the refractive index difference of the molecular species is sufficiently large, one can determine the covering molecule from the associated resonance shift. However, as we will also show below, this method has several drawbacks: The refractive index difference is in fact very small. Also, if both molecular species are present within a certain volume they cannot be distinguished. In contrast, the molecular vibrations are not only more pronounced features, but they also allow for simultaneous detection of the molecular species.

For both methods the recorded spectra are evaluated for every single pixel. A change in the effective refractive index is detected by straightforwardly extracting the resonance position, or transmittance minimum. In order to characterize the strength of the vibrational feature, additional analysis is required. As displayed in Figure 2a, the acquired SEIRA spectra are composed of the plasmon resonance and the vibrational features. The overall spectrum arises due to the coupling of the vibrational mode of the molecules to the plasmonic mode of the antenna, mediated by the near-field enhancement around the antenna. The observed spectrum is therefore the one of a coupled molecule−plasmon system. In order to extract the vibrational (peak-to-peak) signal strength ΔS and thus identify and localize the molecules, a baseline-correction routine is utilized, as introduced by Eilers.[43] The algorithm, which represents a commonly used technique described in detail in previous works,[43,44] reconstructs the uncoupled plasmonic resonance of the antenna. The baseline-corrected spectrum is obtained by dividing the measured raw data by the reconstructed plasmonic resonance. As a result, an uncoupled and baseline-corrected vibrational spectrum with enhanced Fano-type line shape is obtained, as depicted in Figure 2b. For both the refractive index change and the strength of the vibrational feature, this analysis is performed for each spectrum recorded for every individual pixel. Thus, an image of the change in refractive index and of the strength of the vibrational feature can be displayed. This represents in fact *a chemical image*, indicating the spatial distribution of the two molecular species.

In order to verify the plasmonic origin of the discussed features we also irradiated the antennas with perpendicular light polarization. The resulting transmittance spectra, once more depicted for the uncovered, the C_{60}-covered, and the pentacene-covered case, are displayed in Figure 2c. No plasmonic resonance is observed in the displayed wavelength range. The perpendicular plasmonic mode is located at significantly higher frequencies and cannot be excited. None of the spectra show any vibrational features. This fact corroborates the enhanced detection efficiency of the vibrational modes due to the interaction of the molecules with the resonant plasmonic mode. In Figure S1 of the Supporting Information we additionally show the transmittance spectra of pure C_{60} and pentacene films having a thickness of 100 nm, which partially show weak signatures of vibrational modes. By comparing the nonenhanced (shown in Figure S1) to the enhanced vibrational signal strength (Figure 2) we find a 15-fold enhancement. If the number of molecules actively contributing to the signal (i.e., molecules located in the antenna hotspot) are taken into account additionally (according to Vogt et al.),[40] an enhancement factor of roughly 16 000 for the C_{60} vibration at 1430 cm^{-1} is estimated.

Figure 3 illustrates the layout and our measured chemical maps of the pentacene and C_{60}-covered single resonant antenna array sample. Panel 3a shows the visible microscope image of the investigated region. One can clearly distinguish the areas covered with molecular films of 30 nm thickness. As we know the design of the stencil used for the evaporation of the two

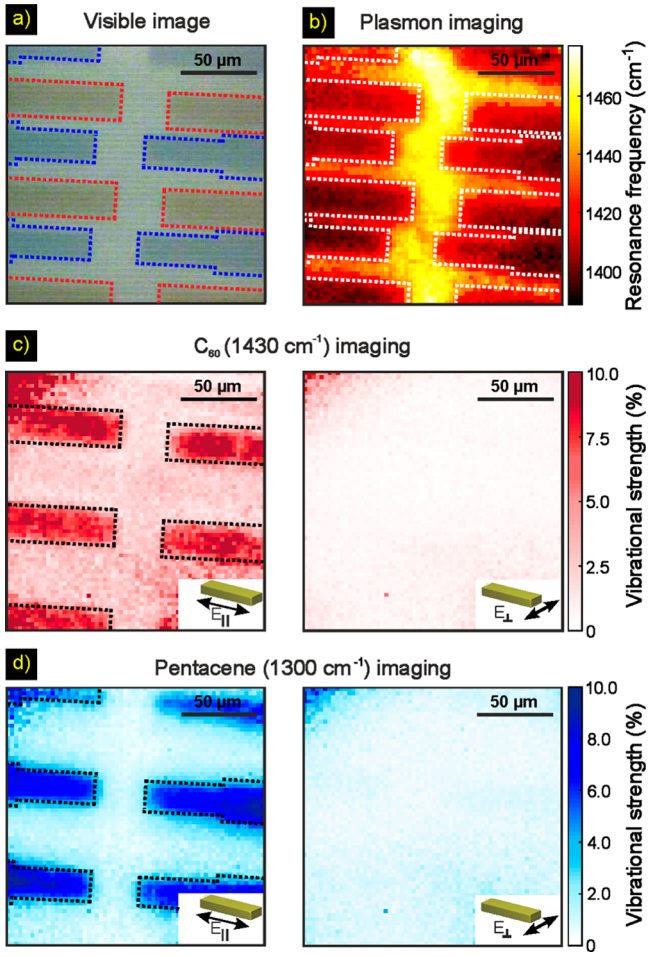

Figure 3. Nanoantenna-enhanced chemical imaging of pentacene and C_{60}. (a) Optical micrograph of the investigated sample area. Darker areas contain nanoantennas covered with microstructured pentacene and C_{60} layers, brighter ones only contain uncovered nanoantennas. As a guide to the eye the molecule-covered areas are outlined with blue (pentacene) and red (C_{60}) dashed lines. (b) Plasmon imaging: Due to the larger effective refractive index of the molecular layers (outlined with dashed white lines), the plasmon resonance of the covered antennas shifts spectrally. The color map indicates the spectral position of the plasmon resonance for every recorded pixel. One can clearly identify the covered areas as regions of smaller resonance frequency when compared with the uncovered areas. However, a *material-specific* identification of pentacene and C_{60} is not possible this way. (c) Chemical imaging of C_{60}: The vibrational signal strength ΔS at 1430 cm^{-1} for parallel (left panel) and perpendicular polarization (right panel) is plotted for each detector pixel. The C_{60}-covered areas are outlined with dashed black lines. If the vibrational signals are resonantly enhanced (parallel polarization) the C_{60} areas can be identified as regions of large ΔS. (d) Chemical imaging of pentacene: The vibrational signal strength ΔS at 1300 cm^{-1} for parallel (left panel) and perpendicular polarization (right panel) is plotted for each detector pixel. The pentacene-covered areas are outlined with dashed black lines. Similar to the C_{60} case, the pentacene-covered areas can be identified as regions of large ΔS.

DOI: 10.1021/acssensors.7b00063
ACS Sens. 2017, 2, 655−662

molecular films, we can assign the different areas to the two molecular species. Without this prior knowledge of the distribution of the two molecular species, we would not be able to unambiguously identify them from the visible microscope image alone. The areas with a blue rim contain a film of pentacene, and the red-rimmed ones are composed of C_{60}. The remaining areas are uncovered antennas.

We examine the case of pure plasmon imaging; that is, we analyze the shift of the plasmonic resonance due to a changing effective refractive index of the medium surrounding each nanoantenna. In Figure 3b we plot the resonance frequency of the plasmonic resonance observed in each of the 4096 pixels as a colored map over their respective spatial position. As a guide to the eye we have outlined the molecule-covered areas with white dotted lines. One can clearly distinguish two different regions, indicated by a consistently higher and lower resonance frequency. As the antennas are homogeneous over the entire field of view, the regions with a smaller resonance frequency must be covered by a larger effective refractive index medium. In fact, these are the regions with molecular layers. It is noteworthy, however, that it is not possible to unambiguously identify the molecular species from the (nonmaterial specific) resonance shift, even though the shift is approximately 10 cm^{-1}. Both the pentacene and C_{60} films show plasmon resonances with a very similar resonance frequency. This observation is expected, as the difference in the refractive indices of these organic compounds is very small. Thus, this plasmonic imaging technique based solely on resonant shifts is not able to offer *molecular recognition*.

We then analyze the spatial distribution of the nanoantenna-enhanced vibrational features. Figure 3c,d depicts the color-coded maps which are obtained when evaluating the strength of the molecular vibrational feature. Again, the spectrum of each of the 4096 individual pixel is analyzed and the extracted strength of the vibrational features for pentacene and C_{60} is color-coded as a function of its respective spatial position. Figure 3c depicts the result for the vibrational feature at 1430 cm^{-1}, which is characteristic for the presence of C_{60}, for incident light polarized along (left) and perpendicular (right) to the long antenna axis. For the plasmon-resonant case on the left one can clearly distinguish two regions on the sample. One is characterized by a large vibrational strength, and the other by vibrational strength close to zero. The first region perfectly overlaps with the microstructured C_{60} films, outlined by the black dotted line. The other region is either covered by the pentacene film or uncovered. These two regions are indistinguishable. As already expected from the findings discussed above in Figure 2c, the vibrational feature and thus the molecular recognition vanishes when switching the plasmonic resonance off, as indicated for the perpendicular case shown on the right. Additional reference measurements without any nanostructure are displayed in Figure S2. The entire measured area is featureless; hence no differences between the three different regions are visible. Figure 3d shows similar results when analyzing the vibrational feature at 1300 cm^{-1}, which is characteristic for pentacene. In perfect analogy to the previous case, we can observe two distinct regions for the resonant case and only a featureless response for the off-resonant case. The regions of the observed large vibrational strength perfectly coincide with the pentacene films. Areas with a priori high vibrational strengths in the upper left and lower right corner of Figure 3c are artifacts resulting from an inhomogeneous illumination of the FPA detector with IR light. Combining these findings demonstrates the ability to identify the spatial location of the two molecular species from the far-field optical response of the plasmonic nanoantennas. The coupling of the vibrational mode to the resonant nanoantennas leads to a strongly enhanced signal that aids in creating a chemical map of the sample. Clearly, this can be obtained neither in the off-resonant case nor for purely plasmon resonance shift imaging.

For many applications it is required to measure and detect material-specific vibrations over a larger spectral range than can be covered by a single plasmonic resonance. Examples are the CH_2 asymmetric stretching vibrations (2926 cm^{-1}) and Amide I vibrations from 1600 to 1700 cm^{-1}. However, to access full chemical information, broadband characterization is required. Our concept can be easily adapted to accommodate this requirement. In the following we use a doubly resonant nanostructure which allows us to access spectrally well separated vibrational modes.[45] We once more use pentacene and C_{60} films evaporated via stencil lithography as model system.

The results of our dual-band nanoantenna-enhanced chemical imaging are displayed in Figure 4. Figure 4a depicts a sketch of the utilized plasmonic structure. We have introduced two nanoantennas of different length and thus two different plasmonic resonances arranged in a single unit cell. Their cross section is 80 × 100 nm^2 with a length of 2.4 and 0.85 μm, respectively. The unit cell is repeated with a periodicity of 3.9 μm in x- and 1.8 μm in y-direction. We have arranged the antennas perpendicular to each other in order to be able to address each resonance individually. Additionally, we use two short antennas per unit cell in order to partially compensate for smaller dipole strength as compared to the longer antenna. As before, a microstructured layer of pentacene followed by a C_{60} layer evaporated using stencil mask lithography. However, to account for the very weak oscillator strength of the vibrational band at 3050 cm^{-1} the layer thickness was increased to 100 nm. Panel a of Figure 4 also depicts the transmittance spectra of the sample for the two polarization directions, revealing the two plasmonic resonances at around 1425 and 2880 cm^{-1} (please note the discontinuity on the frequency axis). One can also clearly identify three characteristic vibrational features at 1180 cm^{-1} (C_{60}), 1300 cm^{-1} (pentacene), and 3050 cm^{-1} (pentacene). However, the vibrational band at 1430 cm^{-1} is hardly visible (only after baseline correction) because of the nonvanishing and non-enhanced vibrational signal originating from molecules located outside the antenna hotspots (see Figure S3). This absorption feature with a Lorentzian line shape superimposes destructively with the enhanced vibration of molecules located in the antenna hotspot. For the vibrational band at 1430 cm^{-1}, an anti-absorption (negative absorption) is present for the enhanced signals due to the perfect energetic match of the molecular and plasmonic excitation.[40] Consequently, the total signal strength, which is detected in the measurements, is reduced. In contrast, for the C_{60} vibration at 1180 cm^{-1} the tuning between antenna and molecular vibration is less perfect, resulting in an asymmetric vibration for the enhanced part. Consequently, the superposition of both effects leads to a signal which is clearly visible in the IR spectra. Therefore, we selected the C_{60} vibration at 1180 cm^{-1} for further analysis. As mentioned before, 100-nm-thick microstructured layers of C_{60} and pentacene were then thermally evaporated using stencil mask lithography. The molecule-covered areas can be identified

DOI: 10.1021/acssensors.7b00063
ACS Sens. 2017, 2, 655−662

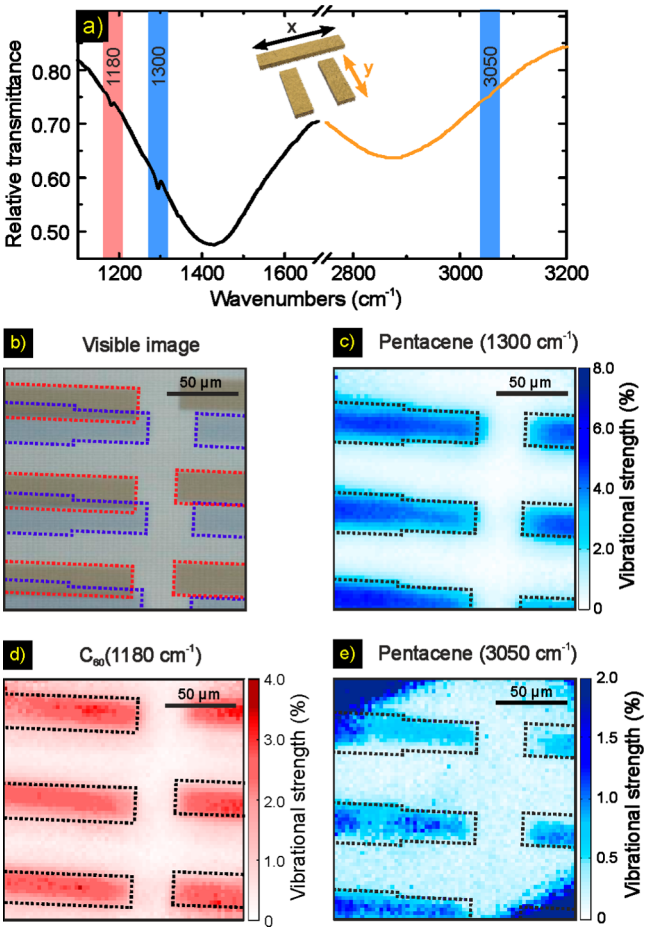

Figure 4. Dual-band nanoantenna-enhanced chemical imaging. (a) Relative IR transmittance spectra of dolmen-shaped nanostructures (see schematic drawing in inset) covered with microstructured areas of pentacene and C_{60}. The plasmon resonances are tuned to the fingerprint (black) and C−H (orange) spectral region. One can clearly identify the characteristic vibrational features of C_{60} at 1180 cm^{-1} and pentacene vibrations at 1300 and 3050 cm^{-1}. No polarizer was used. (b) The visible image depicts the microstructured C_{60} (red) and pentacene (blue) areas with a layer thickness of 100 nm. Locally, pentacene and C_{60} micropatterns overlap resulting in less enhanced vibrations of the upper C_{60} layer due to the spatial confinement of the near-fields (see text). Chemical images of the nanoantenna-enhanced C_{60} and pentacene vibrations in the fingerprint region are shown in (c) and (d). Enabled by the dual-band response of the nanostructures, the C−H vibration at 3050 cm^{-1} can also be imaged (e). Chemical images without nanoantennas feature significantly lower vibrational strengths (compare also SI Figure S3. Please note the different scales in (c) to (e). The dashed lines in (b) to (e) indicate the positions of C_{60} and pentacene as extracted from the visible image and the stencil layout.

in the optical micrograph shown in Figure 4b. Knowing the layout of the stencil, we can distinguish the areas covered with pentacene (outlined in blue) and C_{60} (outlined in red). The two areas partially overlap, with the pentacene layer being the lower one. This results in apparently smaller C_{60} areas compared to the designed ones since the molecular vibrations of C_{60} are less enhanced in the overlap region, due to the spatial confinement of the near-field and vibrational enhancement.[36]

Using the same evaluation routine as discussed above we create the maps depicting the strength of the vibrational features at 1300 cm^{-1} (panel c), 1180 cm^{-1} (panel d), and 3050 cm^{-1} (panel e) for unpolarized excitation. In all three cases we can clearly distinguish two regions, one with a large vibrational signal strength and one with a small vibrational signal strength. These regions perfectly overlap in all cases with the molecule-covered regions as outlined as dashed lines. As discussed for Figure 3c, areas with a priori high vibrational strengths in the upper left and lower right corner of Figure 4e are artifacts. These results clearly demonstrate the capability of dual-band resonant nanoantennas to enhance spectrally separated vibrational modes of two distinct molecular species in IR chemical imaging techniques.

When comparing the results from Figures 3 and 4 as well as when comparing the signal strength observed for the vibrational features at 3050 cm^{-1} with those at 1300 and 1180 cm^{-1}, it becomes apparent that the vibrational signal strength at 3050 cm^{-1} is significantly weaker. There are two distinct reasons for this behavior: First, the plasmon resonance is not perfectly tuned to the vibrational mode. However, a good tuning ratio is indispensable for a maximum signal enhancement. According to previous studies,[40] the enhanced vibrational signal can be roughly twice as large as the observed one in the case of perfect tuning. Second, the near-field enhancement has a λ^3-dependence, therefore dropping off for larger resonance frequencies[46] and reducing the plasmon enhancement which is mainly mediated by the local field strength. However, as is obvious from the map shown in Figure 4e as well as from reference measurements (see Figure S3), the higher frequency vibration of pentacene is still enhanced by the resonant plasmon.

CONCLUSION

To summarize, we employed resonant plasmonic nanoantenna SEIRA to enhance molecular vibrations of C_{60} and pentacene and improved the sensitivity of spectroscopic IR chemical imaging. Based on the enhanced signals, we imaged the lateral spatial distribution of nanometer-thick molecular layers, which was not possible before without antenna enhancement. We demonstrated that resonant SEIRA is able to detect and localize the molecules with molecular distinction. Moreover, dual-band chemical imaging was employed to expand the sensing regime from the fingerprint region to larger wavenumbers. If even higher spatial resolutions below the diffraction limit are desired, near-field optical (SNOM) approaches are the method of choice.[47−49]

In the future, this concept which is straightforwardly extendable to any molecular species, can be exploited for ultrasensitive and selective broadband sensing, e.g., for ultrathin molecular layers for attomolar amounts of molecules, or for biologically or medically relevant samples containing proteins, lipids, and so forth.

ASSOCIATED CONTENT

Supporting Information

The Supporting Information is available free of charge on the ACS Publications website at DOI: 10.1021/acssensors.7b00063.

Chemical images of pentacene and C_{60} with thickness of 30 and 100 nm on a *bare* CaF_2 wafer; single C_{60} and pentacene reference spectra with layer thickness of 100 nm (PDF)

AUTHOR INFORMATION

Corresponding Author

*E-mail: f.neubrech@pi4.uni-stuttgart.de.

DOI: 10.1021/acssensors.7b00063
ACS Sens. 2017, 2, 655−662

ORCID

Frank Neubrech: 0000-0002-5437-4118

Notes

The authors declare no competing financial interest.

■ ACKNOWLEDGMENTS

The authors from the University of Stuttgart acknowledge financial support by the Baden-Württemberg Stiftung (ProteinSens), DFG (SPP1391 Ultrafast NanoOptics), BMBF, and the ERC (COMPLEXPLAS). The authors from Heidelberg University (corporate identity Uni HD) acknowledge financial support from the Heidelberg Graduate School for Fundamental Physics (HGSFP). We thank A. Tittl for nanofabrication of samples for preliminary studies. The authors acknowledge the synchrotron light source ANKA for provision of instruments at the IR2 beamline and would like to thank D. Moss, Y.-L. Mathis, and M. Süpfle for their assistance. The authors from the Max Planck Institute for Solid State Research are grateful to Dr. Florian Letzkus and Prof. Joachim N. Burghartz at the Institute for Microelectronics Stuttgart (IMS CHIPS) for providing high-resolution silicon stencil masks.

■ REFERENCES

(1) Griffiths, P. R.; de Haseth, J. a. *Fourier Transform Infrared Spectrometry*; John Wiley & Sons, Inc.: Hoboken, NJ, USA, 2007.

(2) Barth, A. Infrared Spectroscopy of Proteins. *Biochim. Biophys. Acta, Bioenerg.* **2007**, *1767*, 1073−1101.

(3) Muller, E. A.; Pollard, B.; Raschke, M. B. Infrared Chemical Nano-Imaging: Accessing Structure, Coupling, and Dynamics on Molecular Length Scales. *J. Phys. Chem. Lett.* **2015**, *6*, 1275−1284.

(4) Boldrini, B.; Kessler, W.; Rebner, K.; Kessler, R. Hyperspectral Imaging: A Review of Best Practice, Performance and Pitfalls for Inline and Online Applications. *J. Near Infrared Spectrosc.* **2012**, *20*, 438.

(5) Griffiths, P. R. Infrared and Raman Instrumentation for Mapping and Imaging. In *Infrared and Raman Spectroscopic Imaging*; Wiley-VCH Verlag GmbH & Co. KGaA: Weinheim, Germany, 2009; pp 1−64.

(6) Verdonck, M.; Denayer, A.; Delvaux, B.; Garaud, S.; De Wind, R.; Desmedt, C.; Sotiriou, C.; Willard-Gallo, K.; Goormaghtigh, E. Characterization of Human Breast Cancer Tissues by Infrared Imaging. *Analyst* **2016**, *141*, 606−619.

(7) Petibois, C.; Déléris, G. Chemical Mapping of Tumor Progression by FT-IR Imaging: Towards Molecular Histopathology. *Trends Biotechnol.* **2006**, *24*, 455−462.

(8) Diem, M.; Romeo, M.; Boydston-White, S.; Miljković, M.; Matthäus, C. A Decade of Vibrational Micro-Spectroscopy of Human Cells and Tissue (1994−2004). *Analyst* **2004**, *129*, 880−885.

(9) Nasse, M. J.; Walsh, M. J.; Mattson, E. C.; Reininger, R.; Kajdacsy-Balla, A.; Macias, V.; Bhargava, R.; Hirschmugl, C. J. High-Resolution Fourier-Transform Infrared Chemical Imaging with Multiple Synchrotron Beams. *Nat. Methods* **2011**, *8*, 413−416.

(10) Petibois, C.; Déléris, G.; Piccinini, M.; Cestelli-Guidi, M.; Marcelli, A. A Bright Future for Synchrotron Imaging. *Nat. Photonics* **2009**, *3*, 179−179.

(11) Marcelli, A.; Cricenti, A.; Kwiatek, W. M.; Petibois, C. Biological Applications of Synchrotron Radiation Infrared Spectromicroscopy. *Biotechnol. Adv.* **2012**, *30*, 1390−1404.

(12) Childs, D. T. D.; Hogg, R. A.; Revin, D. G.; Rehman, I. U.; Cockburn, J. W.; Matcher, S. J. Sensitivity Advantage of QCL Tunable-Laser Mid-Infrared Spectroscopy Over FTIR Spectroscopy. *Appl. Spectrosc. Rev.* **2015**, *50*, 822−839.

(13) Yeh, K.; Kenkel, S.; Liu, J.; Bhargava, R. Fast Infrared Chemical Imaging with a Quantum Cascade Laser. *Anal. Chem.* **2015**, *87*, 485−493.

(14) Bassan, P.; Weida, M. J.; Rowlette, J.; Gardner, P. Large Scale Infrared Imaging of Tissue Micro Arrays (TMAs) Using a Tunable Quantum Cascade Laser (QCL) Based Microscope. *Analyst* **2014**, *139*, 3856−3859.

(15) Kröger, N.; Egl, A.; Engel, M.; Gretz, N.; Haase, K.; Herpich, I.; Kränzlin, B.; Neudecker, S.; Pucci, A.; Schönhals, A.; et al. Quantum Cascade Laser−based Hyperspectral Imaging of Biological Tissue. *J. Biomed. Opt.* **2014**, *19*, 111607.

(16) Novotny, L.; van Hulst, N. Antennas for Light. *Nat. Photonics* **2011**, *5*, 83−90.

(17) Bauch, M.; Toma, K.; Toma, M.; Zhang, Q.; Dostalek, J. Plasmon-Enhanced Fluorescence Biosensors: A Review. *Plasmonics* **2014**, *9*, 781−799.

(18) Zhang, R.; Zhang, Y.; Dong, Z. C.; Jiang, S.; Zhang, C.; Chen, L. G.; Zhang, L.; Liao, Y.; Aizpurua, J.; Luo, Y.; et al. Chemical Mapping of a Single Molecule by Plasmon-Enhanced Raman Scattering. *Nature* **2013**, *498*, 82−86.

(19) Schlücker, S. Surface-Enhanced Raman Spectroscopy: Concepts and Chemical Applications. *Angew. Chem., Int. Ed.* **2014**, *53*, 4756−4795.

(20) Das, G.; Mecarini, F.; Gentile, F.; De Angelis, F.; Mohan Kumar, H.; Candeloro, P.; Liberale, C.; Cuda, G.; Di Fabrizio, E. Nano-Patterned SERS Substrate: Application for Protein Analysis vs. Temperature. *Biosens. Bioelectron.* **2009**, *24*, 1693−1699.

(21) Limaj, O.; Etezadi, D.; Wittenberg, N. J.; Rodrigo, D.; Yoo, D.; Oh, S.; Altug, H. Infrared Plasmonic Biosensor for Real-Time and Label-Free Monitoring of Lipid Membranes. *Nano Lett.* **2016**, *16*, 1502−1508.

(22) Abb, M.; Wang, Y.; Papasimakis, N.; de Groot, C. H.; Muskens, O. L. Surface-Enhanced Infrared Spectroscopy Using Metal Oxide Plasmonic Antenna Arrays. *Nano Lett.* **2014**, *14*, 346−352.

(23) Rodrigo, D.; Limaj, O.; Janner, D.; Etezadi, D.; Garcia de Abajo, F. J.; Pruneri, V.; Altug, H. Mid-Infrared Plasmonic Biosensing with Graphene. *Science* **2015**, *349*, 165−168.

(24) Wang, T.; Nguyen, V. H.; Buchenauer, A.; Schnakenberg, U.; Taubner, T. Surface Enhanced Infrared Spectroscopy with Gold Strip Gratings. *Opt. Express* **2013**, *21*, 9005.

(25) Adato, R.; Altug, H. In-Situ Ultra-Sensitive Infrared Absorption Spectroscopy of Biomolecule Interactions in Real Time with Plasmonic Nanoantennas. *Nat. Commun.* **2013**, *4*, 2154.

(26) Huck, C.; Vogt, J.; Sendner, M.; Hengstler, D.; Neubrech, F.; Pucci, A. Plasmonic Enhancement of Infrared Vibrational Signals: Nanoslits versus Nanorods. *ACS Photonics* **2015**, *2*, 1489−1497.

(27) Cerjan, B.; Yang, X.; Nordlander, P.; Halas, N. J. Asymmetric Aluminum Antennas for Self-Calibrating Surface-Enhanced Infrared Absorption Spectroscopy. *ACS Photonics* **2016**, *3*, 354−360.

(28) Aouani, H.; Šípová, H.; Rahmani, M.; Navarro-Cia, M.; Hegnerová, K.; Homola, J.; Hong, M.; Maier, S. A. Ultrasensitive Broadband Probing of Molecular Vibrational Modes with Multifrequency Optical Antennas. *ACS Nano* **2013**, *7*, 669−675.

(29) Hoffmann, J. M.; Yin, X.; Richter, J.; Hartung, A.; Maß, T. W. W.; Taubner, T. Low-Cost Infrared Resonant Structures for Surface-Enhanced Infrared Absorption Spectroscopy in the Fingerprint Region from 3 to 13 μm. *J. Phys. Chem. C* **2013**, *117*, 11311−11316.

(30) Cubukcu, E.; Zhang, S.; Park, Y.-S.; Bartal, G.; Zhang, X. Split Ring Resonator Sensors for Infrared Detection of Single Molecular Monolayers. *Appl. Phys. Lett.* **2009**, *95*, 43113.

(31) Huck, C.; Toma, A.; Neubrech, F.; Chirumamilla, M.; Vogt, J.; De Angelis, F.; Pucci, A. Gold Nanoantennas on a Pedestal for Plasmonic Enhancement in the Infrared. *ACS Photonics* **2015**, *2*, 497−505.

(32) Neubrech, F.; Pucci, A.; Cornelius, T. W.; Karim, S.; García-Etxarri, A.; Aizpurua, J. Resonant Plasmonic and Vibrational Coupling in a Tailored Nanoantenna for Infrared Detection. *Phys. Rev. Lett.* **2008**, *101*, 157403.

(33) Ataka, K.; Stripp, S. T.; Heberle, J. Surface-Enhanced Infrared Absorption Spectroscopy (SEIRAS) to Probe Monolayers of Membrane Proteins. *Biochim. Biophys. Acta, Biomembr.* **2013**, *1828*, 2283−2293.

DOI: 10.1021/acssensors.7b00063
ACS Sens. 2017, 2, 655−662

(34) Hoang, C. V.; Oyama, M.; Saito, O.; Aono, M.; Nagao, T. Monitoring the Presence of Ionic Mercury in Environmental Water by Plasmon-Enhanced Infrared Spectroscopy. *Sci. Rep.* **2013**, *3*, 1175.
(35) Braun, A.; Maier, S. A. Versatile Direct Laser Writing Lithography Technique for Surface Enhanced Infrared Spectroscopy Sensors. *ACS Sensors* **2016**, *1*, 1155−1162.
(36) Neubrech, F.; Beck, S.; Glaser, T.; Hentschel, M.; Giessen, H.; Pucci, A. Spatial Extent of Plasmonic Enhancement of Vibrational Signals in the Infrared. *ACS Nano* **2014**, *8*, 6250−6258.
(37) Chen, C.-K.; Chang, M.-H.; Wu, H.-T.; Lee, Y.-C.; Yen, T.-J. Enhanced Vibrational Spectroscopy, Intracellular Refractive Indexing for Label-Free Biosensing and Bioimaging by Multiband Plasmonic-Antenna Array. *Biosens. Bioelectron.* **2014**, *60*, 343−350.
(38) Zschieschang, U.; Hofmockel, R.; Rödel, R.; Kraft, U.; Kang, M. J.; Takimiya, K.; Zaki, T.; Letzkus, F.; Butschke, J.; Richter, H.; et al. Megahertz Operation of Flexible Low-Voltage Organic Thin-Film Transistors. *Org. Electron.* **2013**, *14*, 1516−1520.
(39) Zaki, T.; Ante, F.; Zschieschang, U.; Butschke, J.; Letzkus, F.; Richter, H.; Klauk, H.; Burghartz, J. N. A 3.3 V 6-Bit 100 kS/s Current-Steering Digital-to-Analog Converter Using Organic P-Type Thin-Film Transistors on Glass. *IEEE J. Solid-State Circuits* **2012**, *47*, 292−300.
(40) Vogt, J.; Huck, C.; Neubrech, F.; Toma, A.; Gerbert, D.; Pucci, A. Impact of the Plasmonic near- and Far-Field Resonance-Energy Shift on the Enhancement of Infrared Vibrational Signals. *Phys. Chem. Chem. Phys.* **2015**, *17*, 21169−21175.
(41) Adato, R.; Yanik, A. A.; Wu, C.-H.; Shvets, G.; Altug, H. Radiative Engineering of Plasmon Lifetimes in Embedded Nano-antenna Arrays. *Opt. Express* **2010**, *18*, 4526.
(42) Knipp, D.; Street, R. A.; Völkel, A.; Ho, J. Pentacene Thin Film Transistors on Inorganic Dielectrics: Morphology, Structural Properties, and Electronic Transport. *J. Appl. Phys.* **2003**, *93*, 347−355.
(43) Eilers, P. H. C. A Perfect Smoother. *Anal. Chem.* **2003**, *75*, 3631−3636.
(44) Huck, C.; Neubrech, F.; Vogt, J.; Toma, A.; Gerbert, D.; Katzmann, J.; Härtling, T.; Pucci, A. Surface-Enhanced Infrared Spectroscopy Using Nanometer-Sized Gaps. *ACS Nano* **2014**, *8*, 4908−4914.
(45) Chen, K.; Adato, R.; Altug, H. Dual-Band Perfect Absorber for Multispectral Plasmon-Enhanced Infrared Spectroscopy. *ACS Nano* **2012**, *6*, 7998−8006.
(46) Weber, K.; Nesterov, M. L.; Weiss, T.; Scherer, M.; Hentschel, M.; Vogt, J.; Huck, C.; Li, W.; Dressel, M.; Giessen, H.; et al. Wavelength Scaling in Antenna-Enhanced Infrared Spectroscopy: Toward the Far-IR and THz Region. *ACS Photonics* **2017**, *4*, 45−51.
(47) Huth, F.; Schnell, M.; Wittborn, J.; Ocelic, N.; Hillenbrand, R. Infrared-Spectroscopic Nanoimaging with a Thermal Source. *Nat. Mater.* **2011**, *10*, 352−356.
(48) Chen, J.; Badioli, M.; Alonso-González, P.; Thongrattanasiri, S.; Huth, F.; Osmond, J.; Spasenović, M.; Centeno, A.; Pesquera, A.; Godignon, P.; et al. Optical Nano-Imaging of Gate-Tunable Graphene Plasmons. *Nature* **2012**, *487*, 77−81.
(49) Woessner, A.; Lundeberg, M. B.; Gao, Y.; Principi, A.; Alonso-González, P.; Carrega, M.; Watanabe, K.; Taniguchi, T.; Vignale, G.; Polini, M.; et al. Highly Confined Low-Loss Plasmons in Graphene−boron Nitride Heterostructures. *Nat. Mater.* **2014**, *14*, 421−425.

DOI: 10.1021/acssensors.7b00063
ACS Sens. 2017, 2, 655−662